JOURNAL OF MATERIALS SCIENCE 26 (1991) 3879–3890

Effects of growth rate on carbides and microporosity in DS200 + Hf superalloy

A. BALDAN
Division of Materials Science and Technology CSIR, P.O. Box 395, Pretoria 0001, Republic of South Africa

The effects of growth rate on the carbide morphology and microporosity were investigated using DS200 + Hf superalloy, between 16.7×10^{-6} and 266.7×10^{-6} m s^{-1}. The fact that the shape factor remained almost unchanged with the growth rate indicates that the shape of the carbide particles does not directly depend on the cooling rate in this alloy. The stability of carbide particles was considered in terms of the interfacial energy between the carbide and matrix interface and the fluctuation of carbide composition. It was observed that the carbide/-γ-matrix interfacial area per unit volume as a function of growth rate remained almost unchanged (especially above 66.7×10^{-6} m s^{-1}), indicating that the rate of coarsening of carbides during solidification is not affected by the carbide/matrix specific interface energy. One of the factors which determines the rate controlling step for the coarsening of carbide particles is suggested to be Ti in the interdendritic and grain-boundary regions, and Hf in the vicinity of the incipient melting region.

1. Introduction

In Ni-base superalloys, carbide formation is required to stabilize the microstructure against high-temperature creep deformation. This is accomplished by the formation of carbide networks at the grain boundaries. These networks inhibit grain-boundary motion, thus increasing creep and stress-rupture properties [1]. This strengthening mechanism is expected to be more apparent at elevated temperatures (0.5 T_m where T_m is the melting point in absolute scale) where the grain-boundary sliding becomes significant [2]. Carbides may also act as an "unpinning" or "unstrengthening" mechanism if they are present as a continuous morphology which creates an easy path for crack propagation. In general, optimum high-temperature properties are obtained when $M_{23}C_6$ type carbides are present as discrete, uniformly distributed particles along the grain boundaries.

The effects of carbides upon high-temperature properties is dependent upon their chemical formula, morphology (or geometry) and location. However, it should also be mentioned that the real effect (harmful⇌beneficial) of the carbides is still being debated. The nature and morphology (shape, size) of carbide phases in a cast Ni-base superalloy depend on its composition, casting parameters and heat treatments.

The carbides in the as-cast condition are usually of MC type having an ordered NaCl f c c structure. The MC carbides consist of the six Group IV and V transition metals: TiC, ZrC, HfC and VC, NbC, TaC [3]. These six compounds are isometric; as mentioned above, they all crystallize in the f c c NaCl-type structure. In addition, they all share the properties of exceptional hardness, high melting point and low thermal conductivity [3]. The composition of the transition metal MC_x (where x represents the carbon-to-metal ratio) changes dramatically without changing the crystal structure; the value of x is in the range 0.5–0.97 [3].

Although the NaCl f c c-type carbides, for example, TiC, NbC or HfC, are very strong and stable, the multi-component carbides found in many of the Ni-base superalloys seem to have a tendency to dissolve or dissociate after long service at high temperature. However, it was observed [4, 5] that in slowly grown crystals of MAR-M200 superalloy, MC carbide precipitates out as equilibrium phases.

The knowledge of the properties of stable carbides, such as volume fraction, distribution, mean size, mean shape factor, interparticle spacing, density, particle–matrix interfacial area or specific perimeter and chemical composition, is very important for design purposes. Fernandez *et al.* [6] investigated the effects of solidification parameters on the final morphology of MC carbide in IN100 single-crystal alloy. It was observed that the average faceted carbide size and the average spacing of the Chinese script-type carbide became refined with increasing growth rate or cooling rate. It was also found that the specific perimeter of the faceted carbide increased with increasing growth rate or cooling rate, which indicated that coarsening was responsible for the final morphology of this carbide.

Microporosity, caused by gas or shrinkage, is a common defect in castings. The presence of microporosity in cast turbine blades is undesirable because it causes an increase in the number of rejected castings and an increase in the scatter of creep-rupture

0022–2461/91 $03.00 + .12

properties. Microporosity formation in Ni-base superalloys can be greatly affected by the casting parameters, and by the chemical composition of the melt [7–9].

The purpose of this work was to investigate and correlate carbide morphology and microporosity with different growth rates in the directionally solidified DS200 + Hf alloy grown along the ⟨0 0 1⟩ crystallographic direction. The nominal composition of this alloy (wt %) is 0.11C, 9.0Cr, 10.0Co, 5.0Al, 2.0Ti, 12.0W, 1.0Nb, 0.015B, < 0.05Zr, 1.75Hf and balance nickel.

2. Experimental procedure

The rod-like specimens along the ⟨0 0 1⟩ crystallographic direction from DS200 + Hf superalloy were unidirectionally solidified. These specimens were prepared under six growth conditions with growth rate, R, varying between 16.7×10^{-6} and 266.7×10^{-6} m s^{-1}. The three specimens from the unidirectionally solidified ingot, taken from top, middle and bottom sections, were selected for metallographic investigations. Optical and scanning electron microscopy were used to investigate the general microstructural features, such as secondary dendrite arm spacing (SDAS), porosity and morphology of carbides. For image analysis a Cambridge instrument, Q520 system, was used to measure the area, perimeter, shape, size and density of carbide particles. For these analyses, six scanning electron micrographs with adjoining fields from the gold-coated samples were taken at a magnification of × 200 for each sample.

Electron microprobe analysis (EMPA) was used to obtain quantitative chemical analysis by wavelength dispersive spectrometry (WDS). X-ray data were converted to compositions using the ZAF correction computer program. The carbon content of the carbides was not measured but simply subtracted from the balance. The X-ray distributions of major elements including Ti, Nb, W and Hf in carbide particles were also recorded.

3. Results

3.1. Carbides

The general microstructural features of carbides are shown in Fig. 1, at two different growth rates, 16.7×10^{-6} and 100×10^{-6} m s^{-1}. These figures illustrate that the carbide morphology shows a similar geometry, and mainly two types of carbide particles, namely, elongated or rod-like type; and more equiaxed, blocky and massive type. A detailed investigation of carbide particles was conducted using a specimen with 100×10^{-6} m s^{-1} growth rate. The results are shown in Figs 2–7, which illustrate the typical carbide morphologies observed at different locations of the specimen, and also the distributions of major elements including Ti, Nb, Hf and W. As can be seen in these figures, some of the carbide particles are faceted (i.e. octahedral or cube-shape morphology). Elongated or rod-like particles were also observed. Carbides were found to be located at the grain boundaries and interdendritic regions. In addition, the carbides associated with the incipient melting regions also existed (Fig. 7). It is interesting to analyse the carbide morphologies in Figs 2–4. The octahedral-shape carbide particle geometry in Fig. 2 suggests that this carbide particle has grown by deposition of {1 1 1} planes along the ⟨0 0 1⟩ growth direction. In Fig. 3 there are two arrow-shaped carbide particles. Note

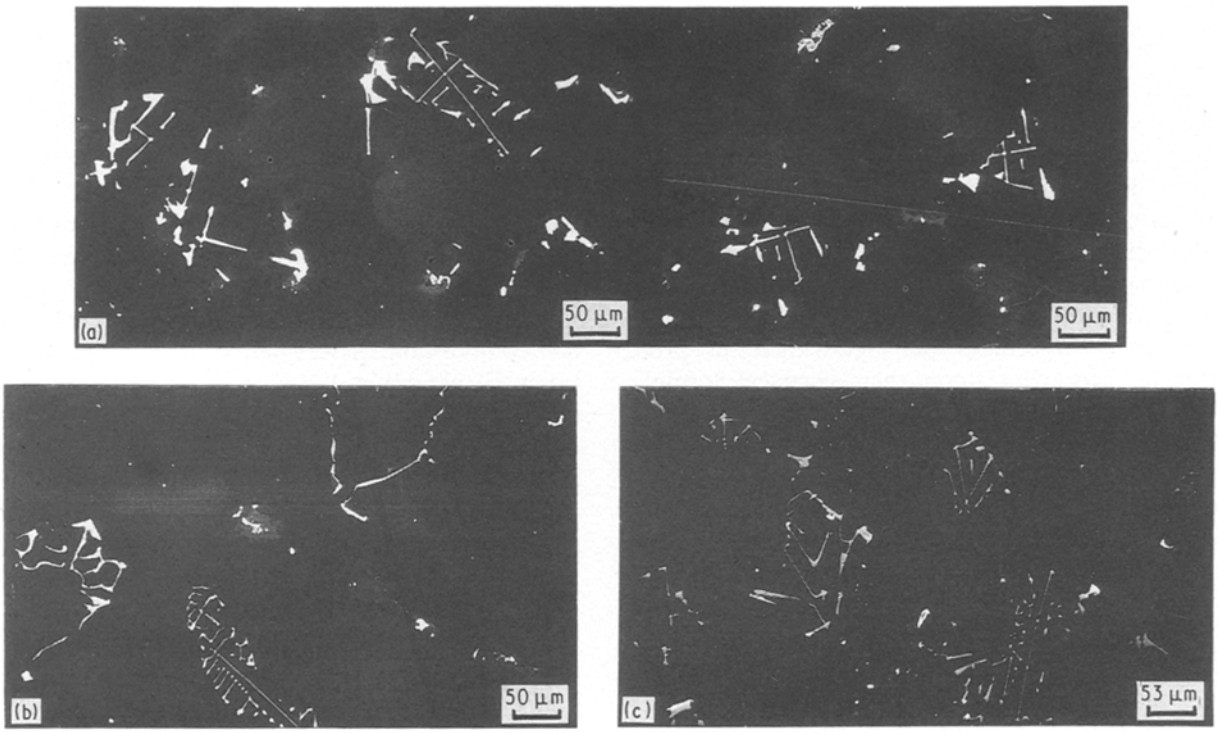

Figure 1 General microstructural features of carbide particles at different growth rates. Note that carbides show similar geometry and mainly two types of particles, namely elongated or rod-like type; more equiaxed and blocky type. (a, b) $R = 16.7 \times 10^{-6}$ m s^{-1}, (c) $R = 100 \times 10^{-6}$ m s^{-1}.

that the growth directions (A–B, C–D) of these particles are suggested to be along ⟨0 0 1⟩ because these particles are aligned perpendicular to each other. The fact that the angle ~ 70° between the arms in Fig. 4 suggests that the two arms of the carbide particles have grown along the ⟨1 1 1⟩ directions. The occurrence of carbide particles with higher energy state such as the rod-like carbide particles along the ⟨1 1 1⟩ directions, indicates the instability of these carbides. In fact they have already started to break into smaller pieces (at A in Fig. 4) in order to reduce the surface-to-bulk energy ratio.

The distribution of elements indicates that the octahedral- and arrow-shaped particles in Figs 2–5 are

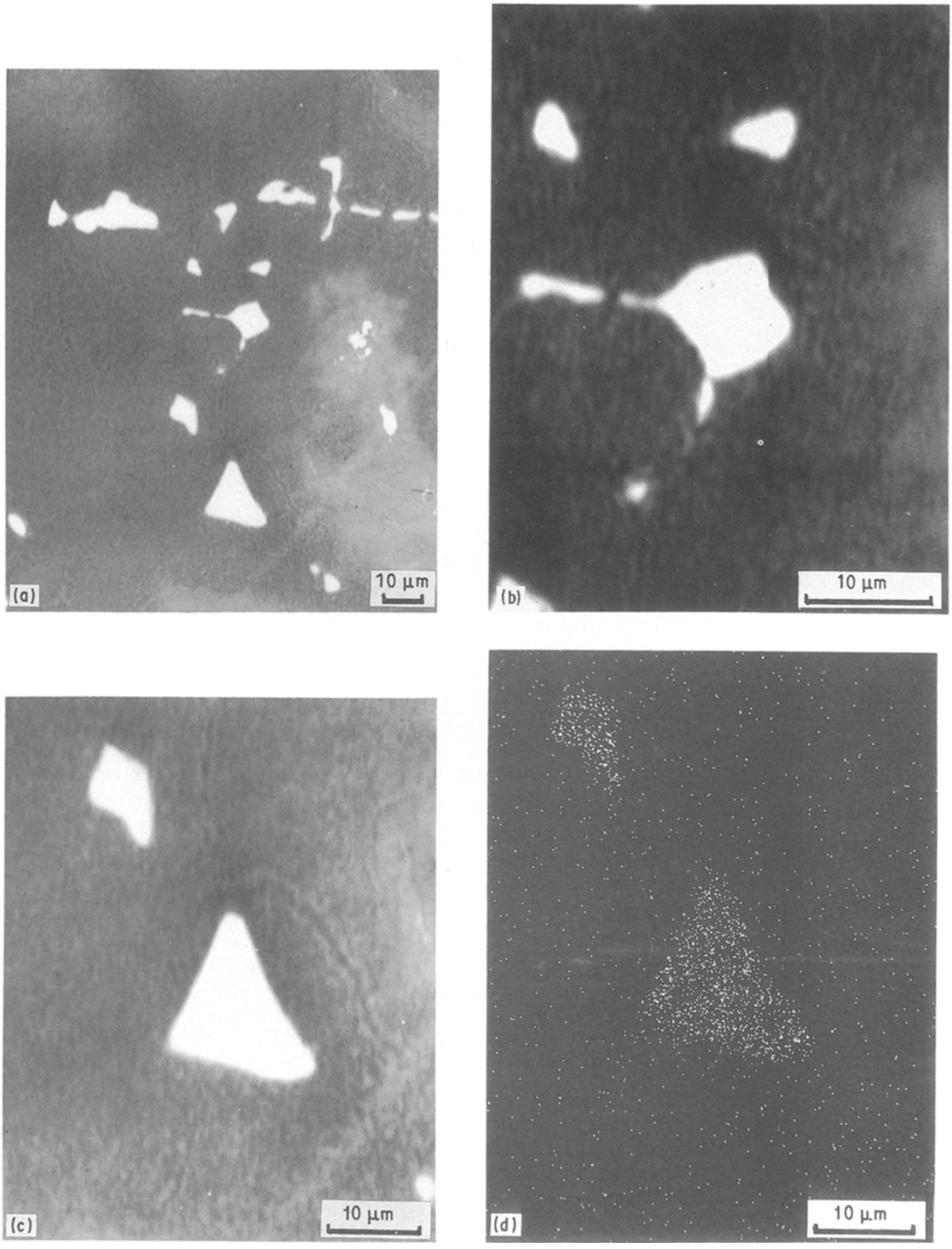

Figure 2 Faceted-type carbide morphology. (a) Rounded cube-like and octahedral-like carbide morphology. (b) Rounded cube-like carbide morphology at higher magnification. (c) Octahedral-type carbide morphology. Elemental distribution of this particle is given in (d)–(f). Note that this particle is enriched in Nb, Ti and to a lesser extent in Hf. (d) Nb. (e) Ti. (f) Hf.

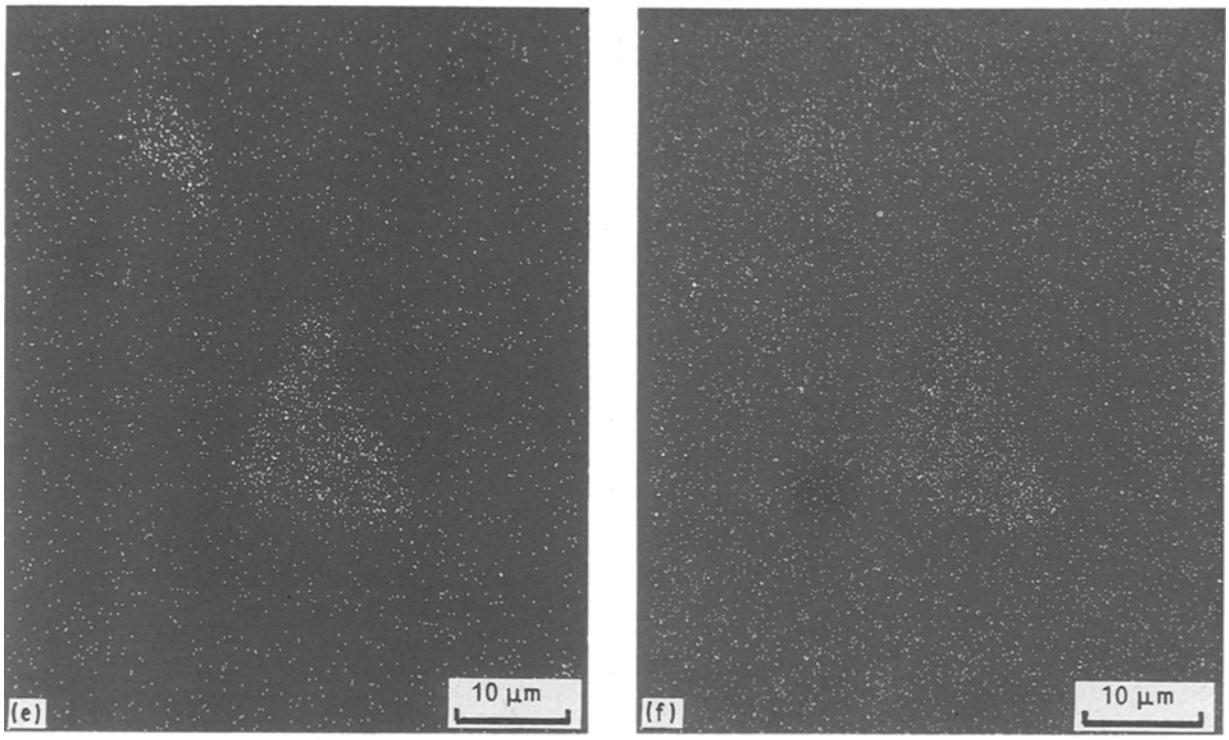

Figure 2 Continued.

(Nb, Ti, Hf)C, (Nb, Hf)C and (Nb, Hf, Ti)C type MC carbides. A blocky-type carbide associated with eutectic pools (Fig. 6) was observed to be ~HfC type. Quantitative analyses by EMPA showed that the following types of carbide (Table I) existed in the alloy with 100×10^{-6} m s^{-1} growth rate: (Ti, Nb)C, (Ti, Nb, Hf)C and ~HfC. In addition, (Cr, W)$_3$C$_2$-type was also observed.

The variations of size, size distribution, shape factor, shape factor distribution, volume fraction, spacing, density, specific perimeter and carbide–matrix interfacial (surface) area of carbide particles with the growth rate, R, are illustrated in Figs 8–16, respectively.

The size of the carbides was measured as the area of an intersected particle on a sectioned plane [10]. The average particle size of carbides refines slowly as the growth rate increases (Fig. 8). The particle size histograms are shown in Fig. 9 for two different growth rates. Examples of these histograms indicate that a significant proportion of particles becomes coarser with decreasing growth rate. Fig. 10 illustrates the mean shape factor as a function of the growth rate. The shape factor, PE, was calculated using the following formula: PE = (perimeter)$^2/4\pi$ (area). As Fig. 10 indicates, the shape factor of carbide particles does not vary with the growth rate. This figure supports the proposal made previously that the shape of the carbide particles does not primarily depend on the cooling rate [11]. The shape factor histograms for the two different growth rates (Fig. 11) show similar trends, also indicating the similarity of distribution of shape factor values for these growth rates.

The volume per cent of the carbides increases from a value of almost 2 at 16.7×10^{-6} m s^{-1} growth rate to ~3.5 at 66.7×10^{-6} m s^{-1}, and further increasing the growth rate the volume fraction seems to become constant within experimental error (Fig. 12).

The average interparticle spacing for carbide particles is illustrated in Fig. 13, which indicates the refinement of interparticle spacing with increasing growth rate. The interparticle spacing, λ, of the carbide was measured using the relation [10]: $\lambda = 0.5/(N_A)^{1/2}$, where N_A is the number of particles per unit area (or the particle density).

As expected from the variation of interparticle spacing, the density of particles increases rapidly up to about 50×10^{-6} m s^{-1} and then becomes almost linear as the growth rate increases (Fig. 14). The variation of specific perimeter or the carbide/γ-matrix interface length per unit area of carbide as a function of growth rate was established in Fig. 15 in order to give an idea about the carbide–matrix interface (surface) area per unit volume of carbide. In this figure the specific perimeter increases very slowly with increasing growth rate, indicating that the final morphology is not controlled effectively by coarsening, which occurs as a result of reduction in the carbide–liquid surface energy. Fig. 16 shows the variation of the carbide–matrix interfacial area per unit volume with the growth rate. This figure indicates that the carbide–matrix interface energy does not vary (especially above about 50×10^{-6} m s^{-1}) with the growth rate, which confirms the trend shown in Fig. 15. The carbide–matrix interfacial area per unit volume of matrix, S_v, was calculated from [10]: $S_v = (4/\pi)L$, where L is the total length of particle outlines per unit area of transverse section.

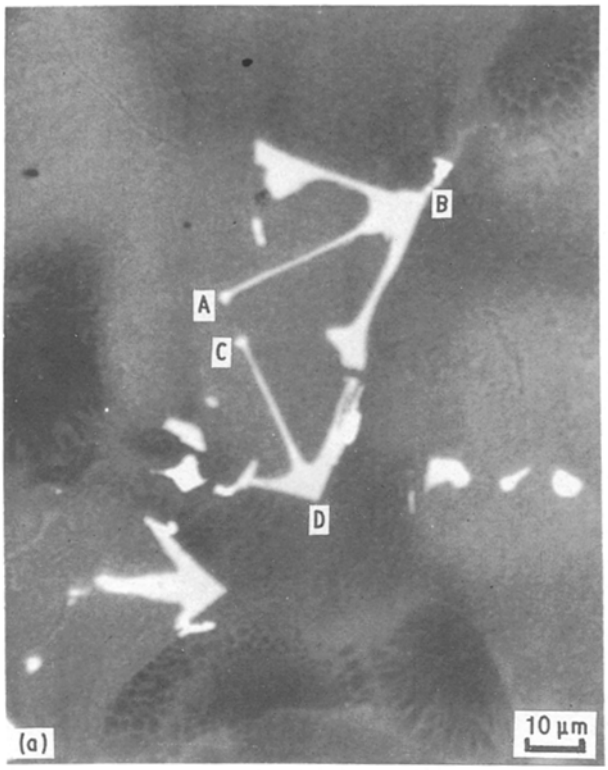

Figure 3 (a) Arrow-shaped carbide morphology. Note that the growth directions (A–B, C–D) of these particles are suggested to be along the ⟨001⟩ because they are aligned perpendicular to each other. The distribution of major elements is given in (b) and (c), which indicates these particles are rich in Nb and Hf. (b) Nb, (c) Hf.

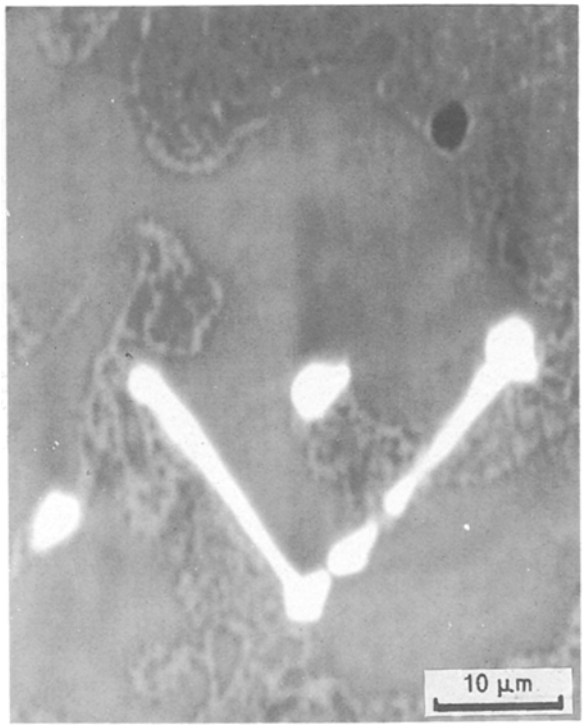

Figure 4 Elongated or rod-like carbide morphology. The fact that the angle between the arms $\simeq 70°$ suggests that the two arms of carbide have grown along the ⟨1 1 1⟩ crystallographic directions.

Figs 17–19 illustrate the effects of variation of the secondary dendrite arm spacing (SDAS) on the average size, average spacing and density of carbide particles, respectively, as a result of variation of growth rate between 16.7×10^{-6} and $266.7 \times 10^{-6}\ m\,s^{-1}$. These figures indicate the refinement of carbide particle geometries with decreasing SDAS. The rather good correlations of carbide geometries with the SDAS will be discussed in Section 4.

3.2. Microporosity

Microporosity formation may be affected by other microstructural constituents such as SDAS, carbides, etc. Therefore, the relationships between the porosity

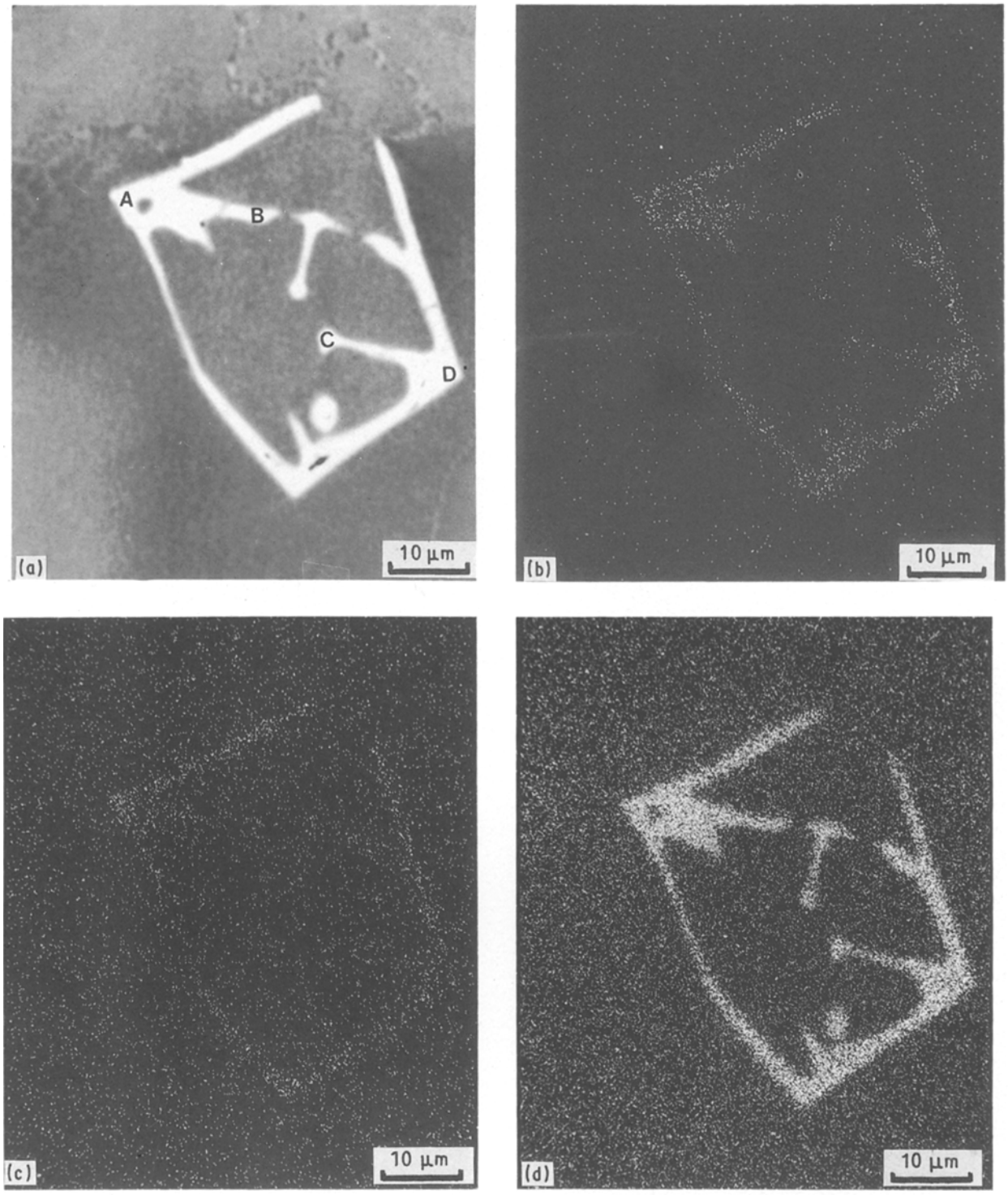

Figure 5 (a) Two arrow-shaped carbide particles joined together to form a complex morphology. Note that their growth directions (A–B, C–D) are parallel. Distributions of major elements are given in (b)–(d), which shows these carbide particles are enriched with Ti, Nb and to a lesser extent with Hf. (b) Nb, (c) Hf, (d) Ti.

level and SDAS, density of carbide particles were established. Fig. 20 indicates a linear relationship between the porosity level and the SDAS; the reduction of porosity level is followed by the refinements of SDAS. On the other hand, there is an inverse linear relationship between the porosity level and density of carbide particles (Fig. 21); increasing the carbide particle density as a result of increasing growth rate reduces the porosity content of the alloy.

4. Discussion

4.1. Carbides

The strength of alloys containing a dispersed second phase, such as carbide particles, generally increases as the geometric (or morphological) parameters (such as the shape factor, spacing, size, density, particle-matrix interface area etc.) of the dispersion are refined. As Figs 17–19 indicate, decreasing the SDAS as a result of increasing growth rate refines the size, spacing and

TABLE I Carbides in as-cast DS200 + Hf alloy grown at 100×10^{-6} m s^{-1}

(Ti, Nb)C	$[Al_{0.01}Ni_{(0.02-0.12)}, Co_{0.02}, Cr_{0.02}, Hf_{(0.10-0.17)}, W_{(0.13-0.17)}, Nb_{(0.31-0.36)}, Ti_{(0.43-0.52)}]C_{(0.69-0.90)}$
HfC	$[Ti_{0.18}, Co_{0.03}, Ni_{0.12}, Nb_{0.27}, W_{0.09}, Hf_{0.69}]C_{0.69}$
(Ti, Nb, Hf)C	$(Ti_{0.37}, Cr_{<0.01}, Co_{0.01}, Ni_{0.06}, Nb_{0.32}, W_{0.13}, Hf_{0.30})C_{0.80}$
$(Cr, W)_3C_2$	$(Al_{0.01}, Co_{0.03}, Ni_{0.11}, Cr_{0.58}, W_{0.24}, Ti_{0.01}, Hf_{0.01}, Nb_{0.02})_3C_2$

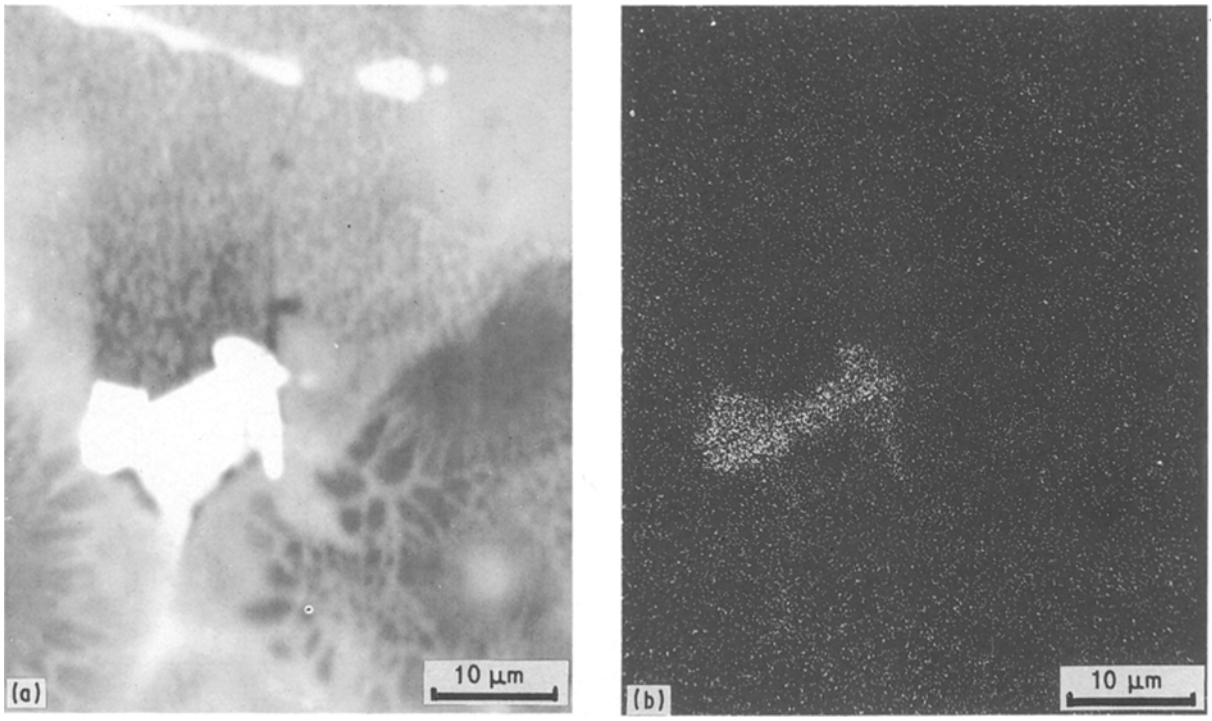

Figure 6 (a) A blocky-type carbide particle in the vicinity of the eutectic pools. Note that this carbide particle is enriched with Hf. (b) Hf.

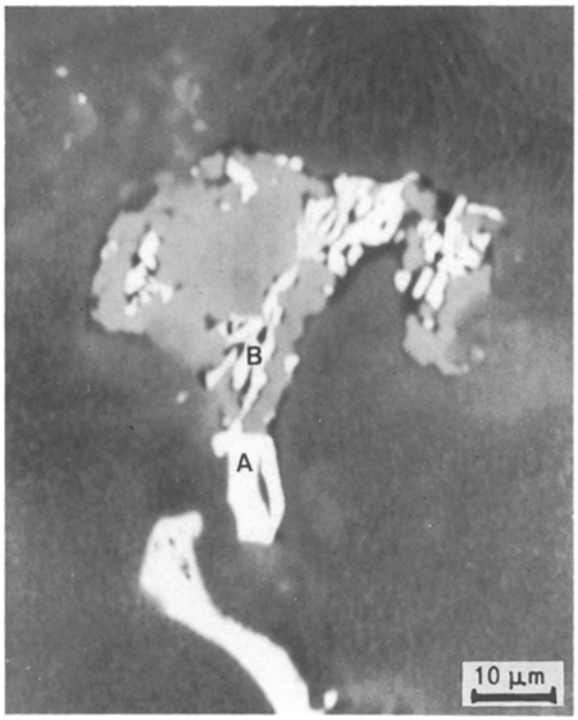

Figure 7 A carbide particle (at A) associated with the incipient melting regions (at B).

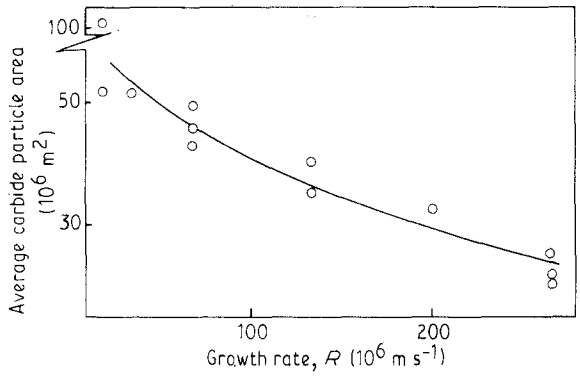

Figure 8 Variation of average carbide particle size (measured as the particle area) with growth rate. Note that the average particle size refines with increasing growth rate.

density of carbide particles, which in turn, it is suggested, increases the strength of DS200 + Hf alloy. Any given particle size is associated with a certain grain size [12], although during rapid thermal cycles there may not always be enough time for the mean grain size, as expected by the Smith/Zener pinning equation, to be achieved. In simplest form, the grain size, $\bar{R}$, is related to the mean particle size, $\bar{r}$, and volume fraction of particles, V_f, as $\bar{R} = 2\bar{r}/3V_f$. This equation was developed by Smith and Zener [12] who assumed that half the particles within a distance of a boundary act in pinning the boundary. It was also assumed that the particle–matrix interfacial energy is uniform for all particles. In the present study, we investigate how we can apply this equation to the carbide particle which shows wide variations in particle-size distributions, and even the compositional fluctuations of carbides shown in particles. In the present investigation there is

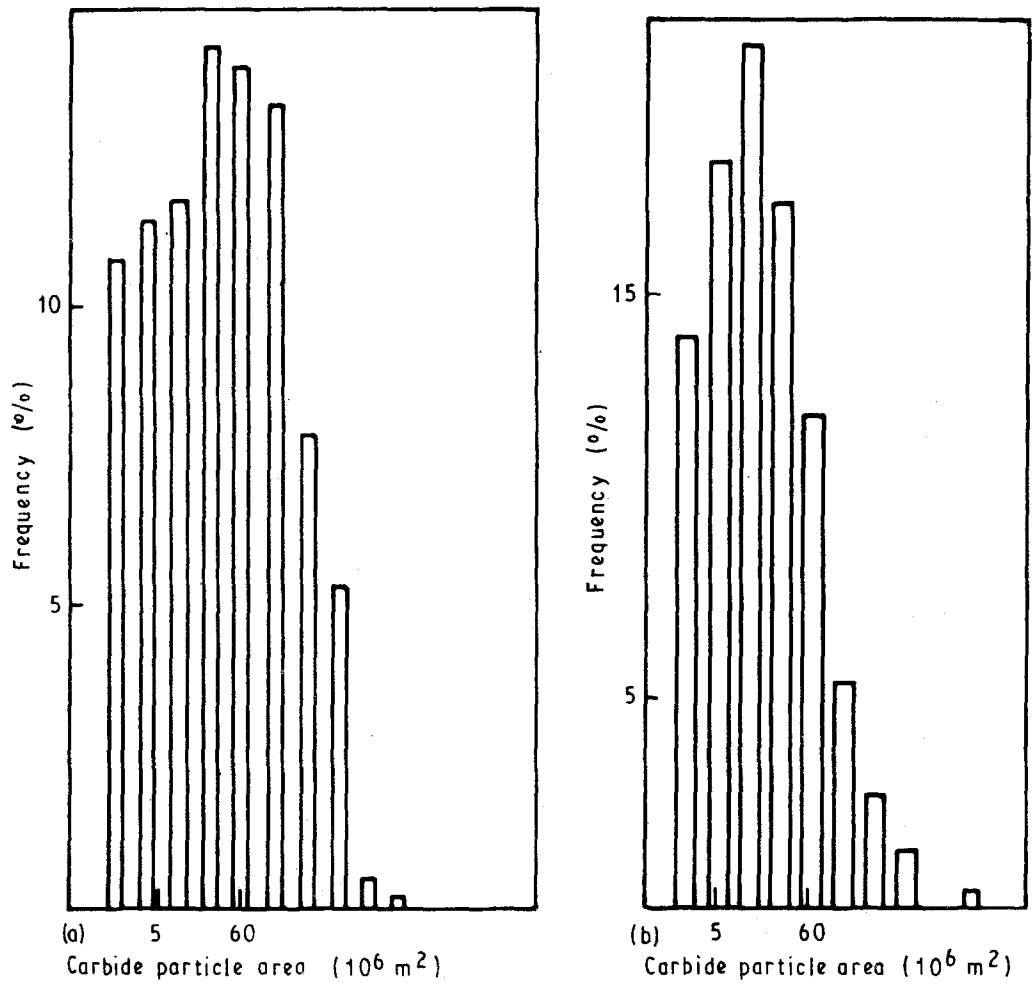

Figure 9 Carbide particle size histograms at two different growth rates. These histograms indicate that a significant proportion of particles becomes coarser with decreasing growth rate. (a) $R = 16.7 \times 10^{-6}$ m s^{-1}, (b) $R = 133.3 \times 10^{-6}$ m s^{-1}.

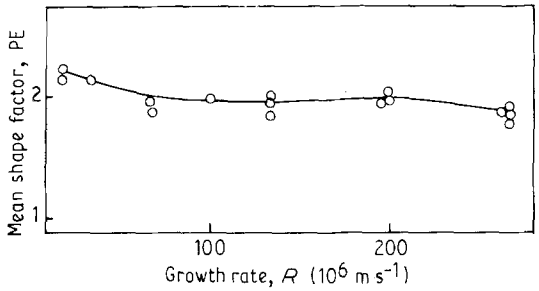

Figure 10 Variation of mean shape factor with growth rate. Note that the mean shape factor remains almost constant with growth rate. When PE = (perimeter)^2/4π (area) = 1 the particle shape is spherical.

a good correlation between the average particle size and the SDAS (see Fig. 17), in which the particle size increases with increasing SDAS. From Figs 17–19 it is possible to consider that the carbide morphological parameters are affected by the SDAS rather than grain size. In other words, the particle size is a "weighing average" measure of SDAS rather than grain size, because SDAS is much finer than the grain size.

At elevated temperatures where dispersed particles have some solubility in the surrounding matrix the larger particles in the dispersion tend to grow in size at the expense of smaller particles. An understanding of the possible mechanisms for this coarsening process, and also the way by which it can be retarded, is important because it is often the Ostwald ripening process which limits the range of application of many dispersion strengthened alloys. The driving force for Ostwald ripening is the net reduction of interfacial energy which occurs when a dispersion of particles coarsens. It is also important to note the initial tendency for coarsening of a dispersion which depends upon the range of particle sizes present within the dispersion. The rate of coarsening can be either interface-controlled (the slowest step is the transfer of atoms across the precipitate/matrix interface) or lattice diffusion-controlled (the slowest step is the diffusion of the migrating species in the matrix phase). By assuming volume diffusion control, it was shown by Wagner [13] and Lifshiftz and Slyozof [14] (the LSW theory) that the following relationship should be obeyed

$$\bar{r}^3 - r_0^3 = Kt \qquad (1)$$

where K is a temperature-dependent rate constant, t is time, $\bar{r}$ is the average particle radius and r_0 is the radius at $t = 0$. The coarsening rate constant K is given by [15]

$$K = \alpha \frac{D\Psi_{int}\Omega^2 C_e}{RT}$$

where D is the "effective" diffusion coefficient, Ω is the

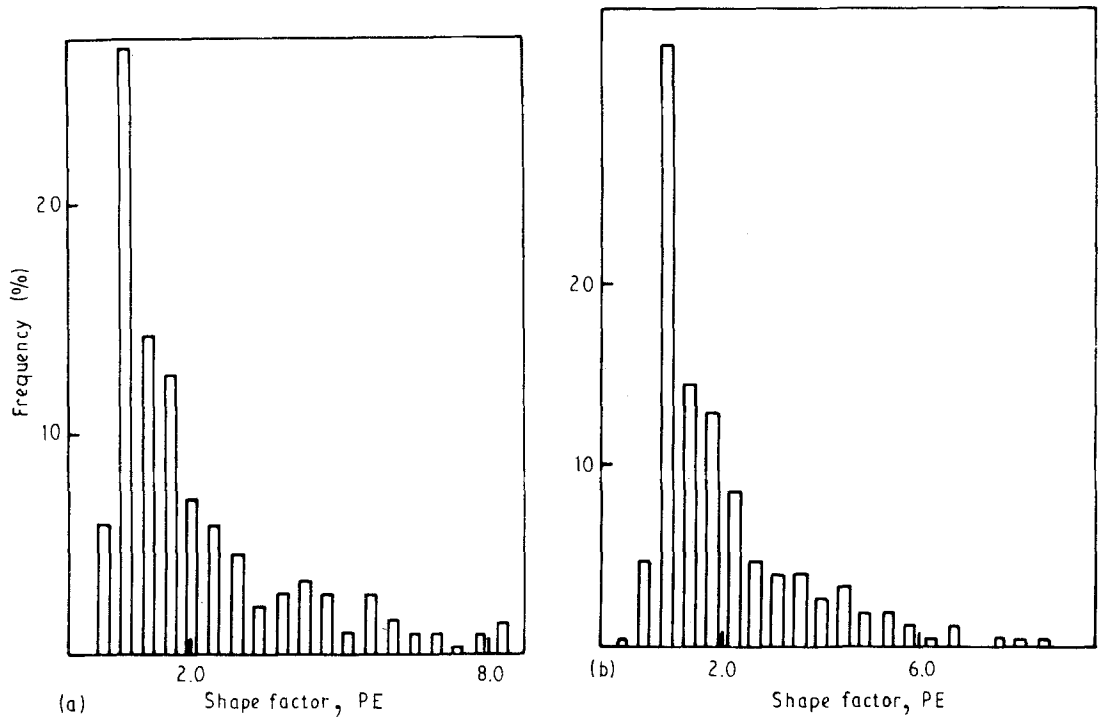

Figure 11 Shape factor distributions (or histograms) at two different growth rates. These histograms show a similar distribution of shape factors at different growth rates. (a) $R = 16.7 \times 10^{-6}\,m\,s^{-1}$, (b) $R = 133.3 \times 10^{-6}\,m\,s^{-1}$.

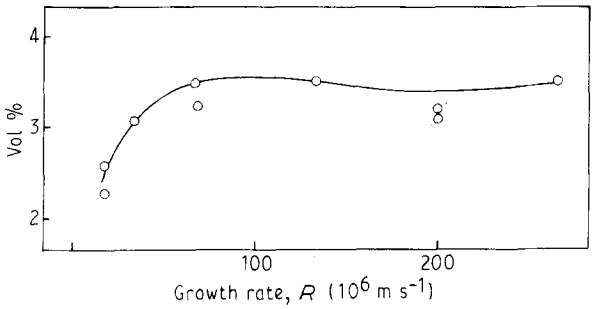

Figure 12 Variation of volume per cent of carbides with growth rate. The volume per cent of carbides remains almost constant above the $66.7 \times 10^{-6}\,m\,s^{-1}$ growth rate, keeping the value at ~ 3.5.

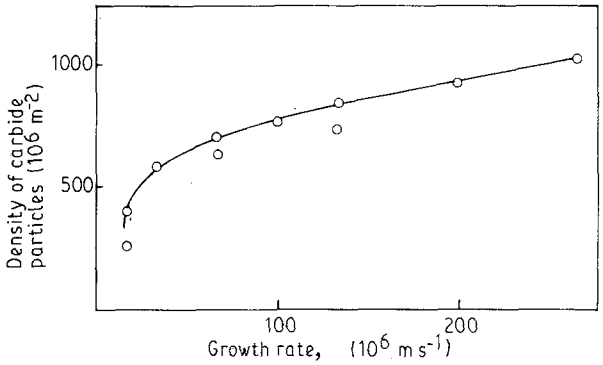

Figure 14 Density of particles increases rapidly up to about $66.7 \times 10^{-6}\,m\,s^{-1}$ and then becomes almost linear as the growth rate increases.

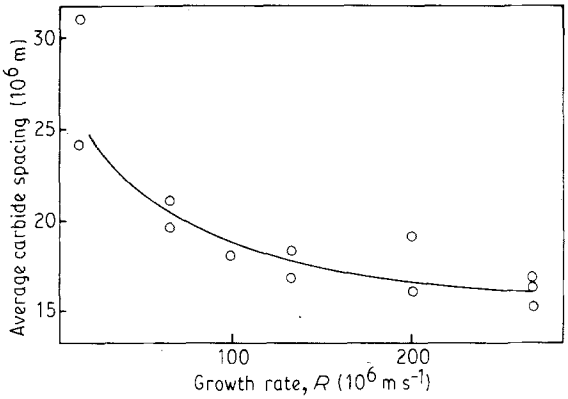

Figure 13 Average particle spacing refines with increasing growth rate.

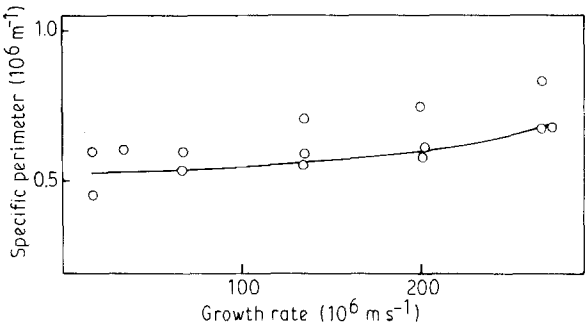

Figure 15 Variation of specific perimeter with growth rate. Specific perimeter increases very slowly with increasing growth rate.

molar volume of the precipitate compound, Ψ_{int} is the specific interfacial (surface) energy of the precipitate–matrix boundary, C_e is the solubility of the rate-controlling element in equilibrium with the largest particles, α is a geometrical constant ($\sim 8/9$ for spheres or cubes), and RT has its usual meaning.

Examination of the above equation indicates that there are three basic compositional parameters, if altered, which can decrease the rate of coarsening, and might retain long-time creep resistance. These are:

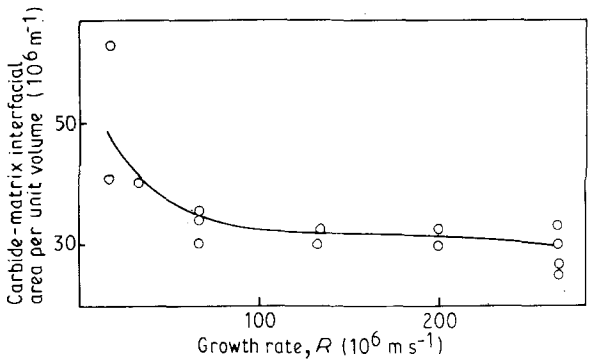

Figure 16 Variation of carbide–matrix interfacial area per unit volume, S_v, with growth rate. S_v remains almost constant above 66.7 $\times 10^{-6}$ m s^{-1}.

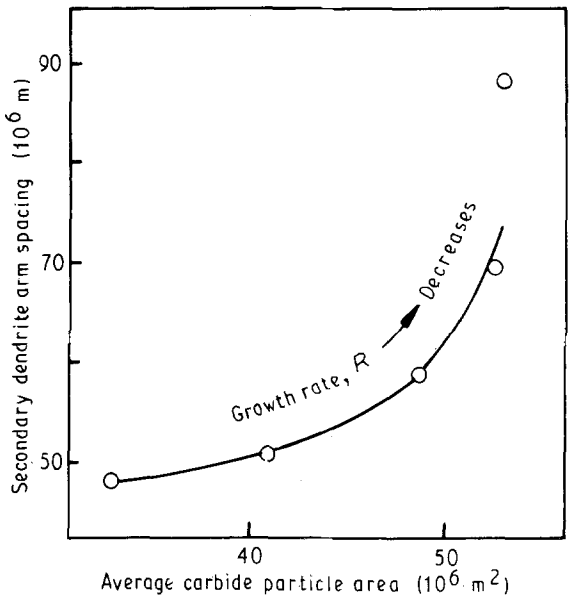

Figure 17 The good correlation between the average carbide size and the SDAS is shown; decreasing the SDAS refines the average carbide size.

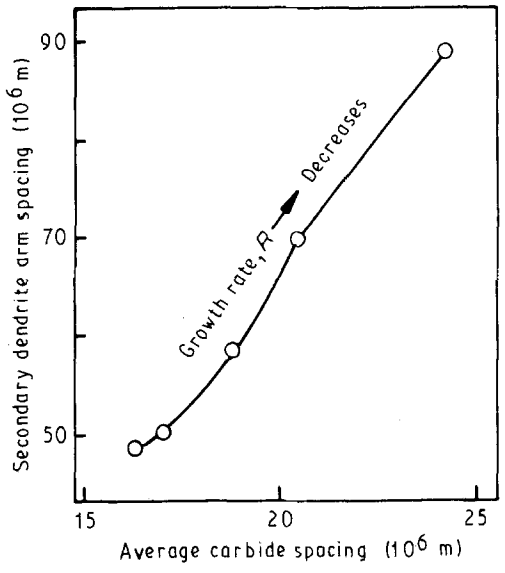

Figure 18 The effects of SDAS on the average carbide spacing. Note that the average carbide spacing refines almost linearly with decreasing SDAS.

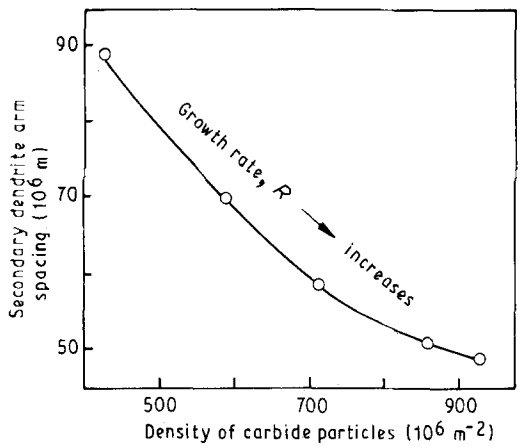

Figure 19 There is an inverse relationship between the density of carbide particles and the SDAS; refining the SDAS increases the carbide particle density.

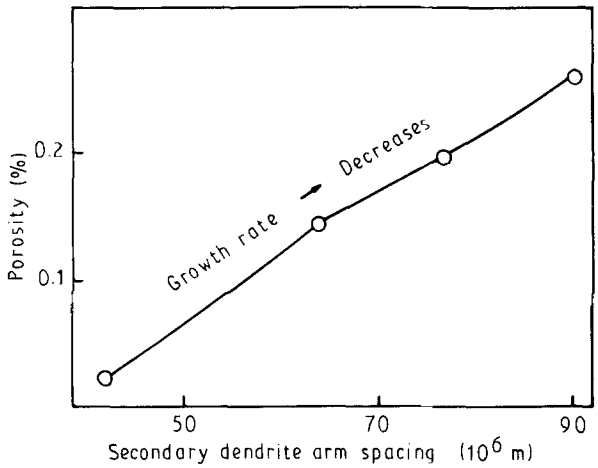

Figure 20 The good correlation between the porosity level and the SDAS; refinement of the SDAS reduces almost linearly the amount of porosity.

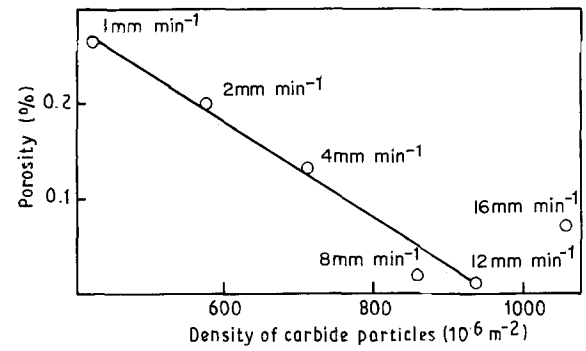

Figure 21 The inverse linear relationship existing between the porosity level and density of carbide particles; increasing the carbide particle density decreases linearly the porosity level.

(i) solute diffusivity, D; (ii) specific interfacial energy for particle/matric boundary, Ψ_{int}; and (iii) solubility of the precipitated phase in the matrix, C_e. Although there is a little information available to guide which compositional variations should be made, theoretically all three of the above parameters (D, Ψ_{int}, C_e) are adjustable in order to minimize the coarsening rate, K, and thereby retard the coarsening. The diffusivity is the diffusion of substitutional solutes which are

most important in the coarsening of MC-type carbides. In the MC carbides investigated in the present study (Table I) and in the past [11, 16], Hf, Ti, Nb and W are the main elements, of which Hf is the most mobile one, because it varied between ~8.5 and 78 wt % in MC carbide [11]. The observations also showed [11] a tendency for the Hf content of carbides in the interdendritic regions, which also has higher Hf segregation [17], to be lowest and to increase in the grain boundaries.

Those carbides in the vicinity of the incipient melting regions, which consist of Ni_5Hf and Ni_7Hf_2 type compounds [18], exhibited the highest Hf content (up to 78 wt %) [11]. However, in the low Hf content region, the most mobile elements, were Ti and Nb, whereas in the high Hf content region the Hf was the most mobile element [11]. In conclusion, it is proposed that the rate-controlling element for coarsening in carbides is Ti in the interdendritic and grain-boundary locations, whereas in the carbides associated with the incipient melting region it is the Hf element which controls the rate of coarsening.

The effect of composition on the interfacial energy, Ψ_{int}, is also complex because Ψ_{int} depends largely upon the degree of coherency at the interface and this varies with the growth of small particles. In general, factors which decrease the interfacial misfit also reduces Ψ_{int} and so decreases the thermodynamic driving force for coarsening. As can be seen in Figs 15 and 16 the growth rate has little effect (especially above 50 $\times 10^{-6}$ m s^{-1}) on the interfacial energy between particle and matrix. As the strain energy around carbide particles must be very small due to the incoherent nature of these particles, the shape of the carbide is primarily determined by the interfacial energy. Therefore, the behaviour of a shape factor as a function of growth rate (Fig. 10) is controlled by the interfacial energy between carbide and matrix, which also has similar behaviour (Figs 15 and 16). In addition, as mentioned in Section 3, the behaviour of the specific perimeter and carbide–matrix interfacial area per unit volume with growth rate, indicates that the interfacial energy does not control effectively the coarsening rate.

The third parameter which controls the coarsening is the solubility, C_e, of the dispersed phase. Solubility depends very strongly upon the free energy of formation, ΔG_f, of the dispersed phase because this is a measure of its atomic bond strength. The values of ΔG_f for many pure carbides are available [19]. The free energy of formation of pure carbides changes with the metal and carbon content [19], indicating also the variation of solubility of carbide particles with carbide contents. Therefore, it is possible that the compositional fluctuations of carbides, which control the free energy of formation, affect the solubility and, in turn, the coarsening rate of carbide particles.

The Hf level in MC carbides determines the solubilities of Ti, Nb and W, and as well as carbon level [11]. Although an increase in Hf results in a decrease in those metallic elements (Ti, W, Nb) in carbides, an increase in the amount of these metallic elements will not increase the volume fraction of carbide particles (Fig. 12).

In conclusion, it is assumed in the LSW equation that the carbide particle coarsening rate, expressed as $(\bar{r}^3 - r_0^3)/t$, is directly proportional to the equilibrium amount of the fastest diffusing metal element involved, namely Hf in carbides associated with the incipient melting region, and Ti in the interdendritic and grain-boundary regions.

4.2. Microporosity

Microporosity formation occurs during the last stages of solidification when capillary feeding becomes insufficient [20]. It was assumed [21] that the maximum size of micropores is a growing function of size of solidification structure. Fig. 20 clearly illustrates the dependence of microporosity content on the SDAS; the porosity level decreases with the refinement of the SDAS. This correlation might also be a manifestation that the porosity level depends on the size of the intergranular and interdendritic area where the liquid metal solidifies last [20]. The investigation of the grain-size dependence of porosity content indicated [20] that porosity exists at the grain boundary and interdendritic area. Because the SDAS is much finer than the grain size, the porosity level is a "weighing average" measure of SDAS rather than grain size [22], as the present result indicates clearly that the porosity level is linearly proportional to the SDAS (Fig. 20). At least two factors have been proposed, which may control microporosity formation in Ni-base superalloys [21]: on the one hand the volume fraction of eutectic liquid at the end of solidification, and on the other hand, a so-called "cork" effect associated with carbides in the case where they form near the liquid temperature.

Although carbon addition is generally thought to increase microporosity incidence in Ni-base superalloy castings [7] it was observed to reduce microporosity in C263 [23] and RENE77 [24] alloys. In the present work, Fig. 21 confirms the above results, in which the porosity level in DS200 + Hf alloy decreases as the density of carbide particles increases. In contrast to common belief [24], this figure also indicates that it is not possible for carbide particles to nucleate on micropore sites because the carbide particle density is inversely proportional to the microporosity content. However, against these observations, the carbon content of IN100 alloy was found to impair the soundness [24]. The contradictory reports indicate that the effect of one specific addition on microporosity incidence in Ni-base superalloy castings depends not only on the nature of the addition but also on the composition of the base alloy [21]. As far as carbon is concerned, it was suggested [24] that microporosity formation was enhanced by increasing amount of primary carbides when forming near the liquidus temperature. Contrary to this suggestion, it was assumed [21] that the amount of primary carbide may improve the soundness of the casting when forming at the very end of the solidification. Certainly in conventional castings, there is also an empirical correlation between the density of blocky carbide and the occurrence of microporosity [25].

5. Conclusions

An investigation of carbide morphology, porosity and SDAS in DS200 + Hf alloy grown at different growth rates (16.7×10^{-6}–266.7×10^{-6} m s^{-1}) has shown the following results.

1. The following types of MC carbide were observed in the alloy grown at 100×10^{-6} m s^{-1}: (Ti, Nb)C, (Ti, Nb, Hf)C and ~HfC. In addition, (Cr, W)$_3$C$_2$-type carbide also existed. The detailed study of carbides showed that mainly two types of morphology existed, namely elongated or rod-like; and more equiaxed and blocky type.

2. The geometric or morphological parameters (size, spacing, density) were refined with increasing growth rate; increasing the growth rate also increases the density and decreases size and spacing of carbide particles.

3. The similar behaviour of the shape factor and the carbide–matrix interfacial area per unit volume (especially above 50×10^{-6} m s^{-1}) as a function of growth rate indicates that the shape of carbide particles is controlled by the specific interfacial (surface) energy between the carbide and γ-matrix boundary.

4. The volume per cent of carbides remains almost constant above the 50×10^{-6} m s^{-1} growth rate, keeping the value at ~3.5.

5. The SDAS controls the morphological parameters of the carbide; decreasing the SDAS refines size, spacing and density of carbide particles.

6. The SDAS also affects the porosity level of the alloy; the refinement of SDAS linearly reduces the porosity level.

7. There is an inverse relationship between the porosity level and the density of carbide particles; increasing the density of carbide particles reduces the porosity level. It was suggested that carbides do not nucleate on the micropore sites.

Acknowledgements

The author acknowledges helpful discussions with Dr N.R. Comins, and the Laboratory facilities provided by the Division of Materials Science and Technology, CSIR, South Africa.

References

1. C. T. SIMS, *J. Metals* **18** (1966) 1119.
2. B. HARRIS and A. R. BONSELL, "Structure and Properties of Engineering Materials" (Longman, New York, NY, 1977) p. 296.
3. W. S. WILLIAMS, *Mater. Sci. Engng* **A105/106** (1988) 1.
4. J. K. TIEN and R. P. GAMBLE, in "Proceedings of the 2nd International Conference on the Strength of Metals and Alloys" (ASM, Metals Park, Ohio, 1970) p. 1037.
5. *Idem, Mater. Sci. Engng* **8** (1971) 152.
6. R. FERNANDEZ, J. C. LECOMTE and T. Z. KATTAMIS, *Met. Trans.* **9A** (1978) 1381.
7. R. M. COOK and A. M. GUTHRIE, *Foundry Trade J.* May 19 (1966) 686.
8. J. CAMPBEL, *The British Foundrymen* April (1969) 147.
9. K. C. ANTONY and J. F. RADOVICH, Proceedings of 3rd International Symposium on Superalloys, Seven Springs, PA, 12–15 September, 1976, edited by B. H. Kear *et al.* (Claiter's Publishing Co.) p. 137.
10. R. T. DEHOFF and F. N. RHINES, "Quantitative Microscopy" (McGraw-Hill, New York, 1968).
11. A. BALDAN and J. M. BENSON, *Z. Metalkde.* **81** (1990) 446.
12. C. S. SMITH and C. ZENER, *Trans. Amer. Inst. Min. Eng.* **175** (1949) 15.
13. C. WAGNER, *Z. Electrochem.* **65** (1961) 581.
14. I. M. LIFSHITZ and V. V. SLYOZOF, *J. Phys. Chem. Solids* **19** (1961) 35.
15. A. BALDAN, "Ostwald Ripening Kinetic Theories and Their Applications to the γ′-precipitates in Ni-base Superalloys" (1988). An unpublished internal report, Division of Materials Science and Technology, CSIR, Pretoria 0001, South Africa.
16. *Idem, Z. Metallkde* **80** (1989) 635.
17. *Idem, J. Mater. Sci.* **25** (1990) 4054.
18. *Idem, ibid.* **25** (1990) 4341.
19. L. E. TOTH, "Transition Metal Carbides and Nitrides" (Academic Press, New York, 1971).
20. E. CHANG and J. C. CHOU, *AFS Trans.* **168** (1987) 749.
21. E. BACHELET and G. LESOUT, "Quality of Castings of Superalloys, High Temperature Alloys for Gas Turbines" (Applied Science, London, 1978) p. 665.
22. M. R. EDWARDS, Proceedings of 4th International Symposium on Superalloys, Seven Springs, PA, 21–25 September, 1980, edited by J. K. Tien, S. T. Wlodek, Hugh Marrow III, M. Gell and G. E. Maurer (American Society for Metals, Metals Park, Ohio) p. 295.
23. F. WETS, "Cost 50 round 1 (FS)" Technical Report SNECMA YORP 20–390 (November 1977).
24. L. OUICHOU, G. LESOULT, G. LAMANTHE, R. HAMAR, J. M. THERET and E. BACHELET, in "Engineering Meeting, High Temperature Alloys for Gas Turbines 1982", Proceedings of a Conference, Liege, Belgium, 4–6 October, 1982, edited by R. Brunetaud, D. Coutsouradis, T. B. Gibbons, Y. Lindblom, D. B. Meadowcroft and R. Stickler (Riedel Publishing Co., Dordrecht, Holland) p. 955.
25. P. N. QUESTED and M. McLEAN, *Mater. Sci. Engng* **65** (1984) 171.

Received 19 March
and accepted 6 November 1990